Scanning transmission proton microscopy tomography of reconstruction cells from simulated data

ZHANG Conghua[1,2,*] LI Min[1] HOU Qing[1]

[1]*Key Laboratory of Radiation Physics and Technology*, *Ministry of Education*, *and the Institute of Nuclear Science and Technology*, *Sichuan University*, *Chengdu 610064*, *China*

[2]*Radiation Division*, *National Institute of Measurement and Testing Technology*, *Chengdu 610021*, *China*

Abstract For scanning transmission proton microscopy tomography, to compare cell images of the proton stopping power and relative electron density, two cell phantoms are designed and simulated by code FLUKA. The cell images are reconstructed by the filtered back projection algorithm, and compared with their tomography imaging. The images of stopping power and relative electron density slightly vary with proton energies, but the internal images are of clear with high resolution. The organic glass image of relative electron density reveals the resolution power of proton tomography. Also, the simulation results reflect effects of the boundary enhancement, the weak artifacts, and the internal structure border extension by multiple scattering. So using proton tomography to analyze internal structure of a cell is a superior.

Key words Monte Carlo simulation, Proton tomography, Cell image, Image quality

1 Introduction

Observing the internal structure of cells is a major issue in biology and medicine[1], while biological cell imaging is available currently[2]. Scanning transmission proton microscopy tomography (STPMT), as an emerging technique of high-contrast, low-dose and low-noise for non-destructive analysis of the cell specimen[3–15], has an potential for producing the structural images of cells[5–7,11,13]. On passing through a sample along an approximately straight-line path of MeV proton microbeams, energy loss of the protons can be measured. The data can be used to reconstruct internal structure of the cell sample and elemental mapping can be done by particle induced X-ray emission (PIXE)[11].

In this paper, we aim at comparing the STPMT cell imaging using the proton stopping power with the electron density. The proton beam imaging is simulated by the Monte Carlo code of FLUKA. The proton energy loss and the electron density integral, as the projection of CT reconstruction[16–19], are used to rebuild the internal structure of the cell, thus revealing the capacity of STPMT reconstruction.

2 Principle of STPMT

The principle of proton imaging was presented with the back projection algorithm and parallel scanning geometries. The discrete sampling with convolution filtering was provided for computer implementation of this algorithm in the tomographic reconstruction.

2.1 Principle of proton imaging

The X-ray computed tomography (CT) imaging based on the X-ray linear attenuation is characterized by Beer Law, describing the intensity reduction as a function of path length, X-ray energy and material linear attenuation coefficients:

$$\phi(L) = \phi_0 \mathrm{e}^{\int_0^L -\mu(E)\mathrm{d}l} \quad (1)$$

Supported by National Natural Science Foundation (No.10775101)

* Corresponding author. *E-mail address:* conghuazhang@sohu.com

Received: 2010-12-05

where ϕ_0 is intensity of the incident X-ray, $\phi(L)$ is intensity of the final X-ray at the position L, and $\mu(E)$ is the linear attenuation coefficient of the X-ray in the specimen. Then intensity ratio (S_x) of the initial X-ray versus final X-ray can be expressed as

$$S_x = \ln(\phi_0/\phi(L)) = \int_0^L \mu(E)\mathrm{d}l \,. \tag{2}$$

The S_x is referred to as projection. The $\mu(E)$ is calculated by the back projection reconstruction algorithm.

Energy loss of the incident protons, caused by inelastic collision of the protons with electrons in the specimen[9], is described by Bethe-Bloch-equation, and defined as[17,18]:

$$\begin{aligned}\Delta E &= \mathrm{E}_{in} - E = -\int_0^L \mathrm{d}l(\mathrm{d}E(l)/\mathrm{d}l) \\ &= \int_0^L S(l, E(l))\mathrm{d}l\end{aligned} \tag{3}$$

where $\mathrm{E_{in}}$ is energy of the incident proton, $E(l)$ is proton energy at the position l, and $-\mathrm{d}E(l)/\mathrm{d}l$, or $S(l,E(l))$, is the linear stopping power at $E(l)$.

Comparing Eq.(2) with Eq.(3), the energy loss can be used to reconstruct the average stopping power and electron density with the back projection reconstruction method (BPRM)[20]. In principle, the distribution of relative electron density in proton beam direction is calculated by measuring the proton energy loss.

According to Bethe-Bloch theory, the stopping power $S(l,E(l))$ can be expressed by as[17,18],

$$\begin{aligned}S(l, E(l)) &= -\frac{\mathrm{d}E(l)}{\mathrm{d}l} \\ &= \eta_{\mathrm{e}}(l) f[I(l), E(l)]\end{aligned} \tag{4}$$

where $\eta_{\mathrm{e}}(l)$ is the relative electron density at the position (l), and $I(l)$ is the mean ionization potential of the specimen. By disregarding the shell correction and the density effect correction, the $f[I(l), E(l)]$ can be calculated by Eq.(5)[17,18],

$$f[I(l), E(l)] = K\frac{1}{\beta^2(E)}\left[\ln\left[\frac{2m_{\mathrm{e}}\mathrm{c}^2\beta^2(E)}{I(l)[(1-\beta^2(E)]}\right] - \beta^2(E)\right] \tag{5}$$

where $\beta(E)=[1-E_0/(E-E_0)^2]^{1/2}$ is the proton velocity relative to the light velocity c in vacuum, $m_{\mathrm{e}}\mathrm{c}^2$ is the electron rest energy, E_0 =938.27 MeV is the proton rest energy, $K= 4\pi r_{\mathrm{e}}\mathrm{m_e c^2}\rho_{\mathrm{e,water}}$, and r_{e} is the classical electron radius (2.818×10^{-13} cm).

$I(l)$ is unknown in STPMT. However, for biological tissue the variation of $I(l)$ is relatively small and the dependence of the $f(I, E)$ on $I(l)$ is relatively weak due to the logarithmic function. Therefore, $I(l)$ can be replaced by the mean ionization potential of water I_{water}=61.77eV. The $f(I,E)$ can be calculated for $E(l)$ at the position l. Eq.(4) can be integrated after separating variables[17,18]:

$$\int_L \eta_{\mathrm{e}}(l)\mathrm{d}l = \int_{E_{\mathrm{out}}}^{\mathrm{E_{in}}} \frac{\mathrm{d}E}{f(I_{\mathrm{water}}, E)} \tag{6}$$

where the left integration is performed by in- and out-going proton energy (E_{in} and E_{out}) along the proton path L. Eq.(6) is in the format of the Radon transform, thus reconstructing the relative electron density $\eta_{\mathrm{e}}(l)$.

2.2 Tomography reconstruction

The back projection algorithm for imaging reconstruction of the parallel proton beam is described as follows[21]. Defining $g(s,\theta)$ as the parallel projection of an image $G(x,y)$ at the location (s,θ) in a polar coordinate system, Eqs.(3) and (6) can be combined into Eq.(7),

$$g(s,\theta) = \begin{cases} \Delta E \\ \int_L \eta_{\mathrm{e}}(l)\mathrm{d}l = \int_{E_{\mathrm{out}}}^{\mathrm{E}_{in}} \frac{\mathrm{d}E}{f(I_{\mathrm{water}}, E)} \end{cases} \tag{7}$$

The filtered projection at the sampled points is calculated by the discrete convolution in Eq.(8).

$$G'(ld, n\Delta\theta) = d\sum_{m=-(M-1)/2}^{(M-1)/2} g(md, n\Delta\theta)h[(l-m)d] \tag{8}$$

where, $G'(ld,n\Delta\theta)$ is the filtered projection at the point $(ld,n\Delta\theta)$, $\Delta\theta$ is the angular sampling interval in 2π, $\Delta\theta = 2\pi/N$ (radians/sample), d is the sampling interval length, l is the discrete number of the sampling distance s, $l=s/d$, M is the total number of the sampling points, and $h[(l-m)d]$ is the transfer function of a filter with which the projection must be processed. The $h[(l-m)d]$ is given by,

$$\begin{aligned}h[(l-m)d] &= 2/\{\pi^2 d^2[1-4(l-m)^2]\} \\ |\ l-m| &\le (M-1)/2\end{aligned} \tag{9}$$

Given the filtered projection, the image $G(x, y)$ is reconstructed by the discrete Eq.(10),

$$G(x,y)=G(ld,n\Delta\theta)=\int_0^{2\pi}G'(ld,n\Delta\theta)\mathrm{d}\theta \approx \Delta\theta\sum_{n=0}^{N-1}G'(ld,n\Delta\theta) \quad (10)$$

According to the Eqs.(7), (8) and (10), the proton energy loss can be used to reconstruct $S(l,E(l))$ and $\eta_e(l)$ distribution in a cell.

3 Simulation models

3.1 Cell models for STPMT

Two cell models, and the experiment configuration, are used to analyze characteristics of STPMT by Monte Carlo simulation, using $S(l,E(l))$ and $\eta_e(l)$ to simulate the proton transport process in cells. The cell model referred as PMMA is a Φ100 μm×100 μm water cylinder containing four PMMA cylinders (Fig.1) suitable for examining spatial resolution of STPMT. With a density of 1.18 g·cm^{-3}, PMMA is also a suitable choice for the density resolution against water. Another cell model of the same geometry has four small cylinders of calcium. Referred as Calcium, it is of greater density, so as to observe contrast image of STPMT. In geometric sizes that are comparable to biological cells, the two models can be used to assess the characteristics of STPMT.

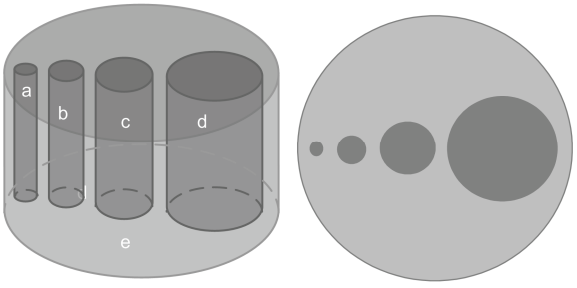

Fig.1 The cell model with four 100-μm cylinders (PMMA or calcium) of Φ5 μm (a), Φ10 μm (b), Φ20 μm (c) and Φ40 μm in a water cylinder of Φ100 μm×100 μm (e).

3.2 Simulation setup

The average energy loss of the in-going proton is obtained by the code FLUKA, and the filtered back projection algorithm is used to reconstruct cell images. Proton beams of 120 μm×120 μm in beam spot and 3, 5 or 7 MeV in energy, enough to cover and penetrate the two models, are rotated around the cell model center, with an angular interval of 1º, to record the projection images. The projection images of 120 μm × 120 μm are divided into 600×600 detector pixels. The sampling number of incident protons for each beam angle is 10^6.

4 Results and Discussion

4.1 Comparison of projection

The 300th segments of the simulated proton energy loss are extracted (Fig.2). Briefly, the contrast of proton energy loss in PMMA cell decreases with increasing incident proton energy. For such an experimental configuration, using energy loss of 3 MeV protons can achieve better imaging results of the models. At 3 MeV, the energy loss contrast is clear (Fig.2a), while the contrast is not so obvious at 5 and 7 MeV (Figs.2b, and 2c). From Fig.2(g) of a 180º scanning, the contrast at 3 MeV well reflects structures of the PMMA cylinders due to different levels of energy loss contrast. This shows a strong resolution capability of the energy loss to distinguish materials in densities close to water.

For calcium cell, the contrast of the proton energy loss on scanning is similar with the PMMA cell at 3, 5 and 7 MeV, as shown in Figs.2(d), (e), (f) and (h).

4.2 Comparison of reconstruction imaging

Fig.3 shows the tomography images of the two cell models, and their internal structures were reconstructed with the filtered back projection principle, based on the proton stopping power and the relative electron density.

At the same proton energy loss, the reconstructed images of the stopping power and the relative electron density are similar, revealing the four small cylinders and their sharp edges, with the image boundaries having obvious enhancement to improve their perceived sharpness or acutance. At 3 MeV, the artifacts of the relative electron density image are more obvious (Fig.3a, and 3g). The artifacts, however, can be possibly filtered by some type of image smoothing filters or corrected.

At the same incident energy and energy loss of the protons, the stopping power images are of higher contrast than the electron density images. The higher energy protons have smaller dE/dx in the model, hence the decreased contrast of the reconstructed images. At 7 MeV, the normalized images of the stopping power and the electron density are almost the same, for either PMMA or calcium, as shown in Figs.3(c), (f), (i) and (l). Figs.3(a) to 3(c), or 3(d) to 3(f), show that the image contrast decreases with increasing energies, with reducing artifacts.

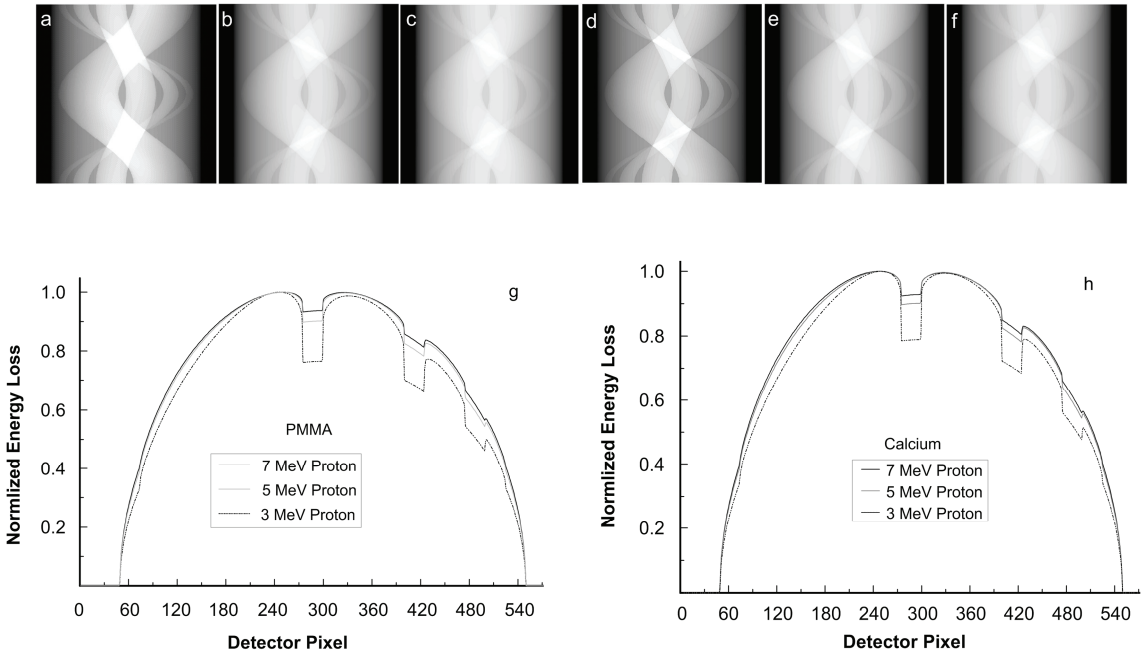

Fig.2 Energy loss of 3, 5 and 7 MeV protons and the 180º scanning for the PMMA model (a, b, c and g); and energy loss of 3, 5 and 7 MeV protons and 180º for the Calcium model (d, e, f and h). A low gray scale indicates low energy loss of proton.

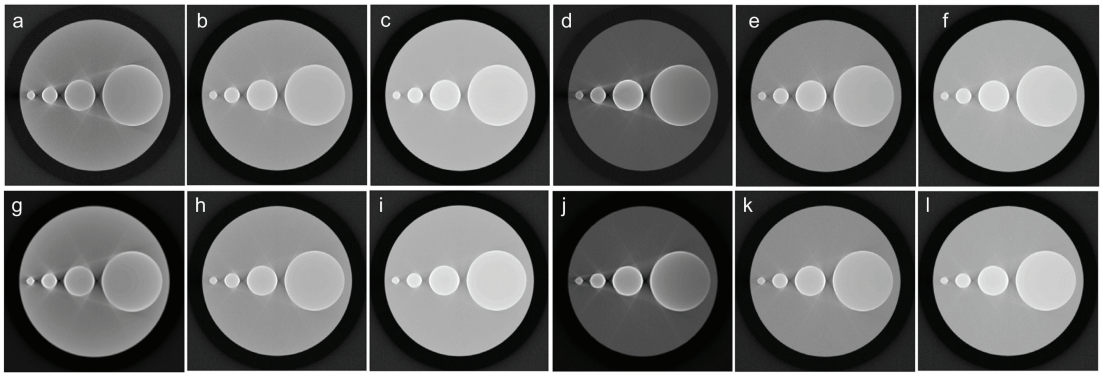

Fig.3 Reconstructed images of relative electron density for the PMMA model with proton beams at 3, 5 and 7 MeV (a, b, and c), and for the Calcium cell with proton beams at 3, 5 and 7 MeV (g, h and i); and reconstructed images of stopping power for PMMA at 3, 5 and 7 MeV (d, e, and f) and Calcium at 3, 5 and 7 MeV (j, k and l).

In Fig.4, the profiles along the horizontal central line are extracted by comparing the similarity of Figs.3(i) with (l), indicating the high contrast in smooth areas and image enhancement effect in the edge of the cell internal structures. The normalized data for the pixel distribution is a significantly difference between the stopping power and the relative electron density, and the electron density image at location 1 and 4 has a better symmetry.

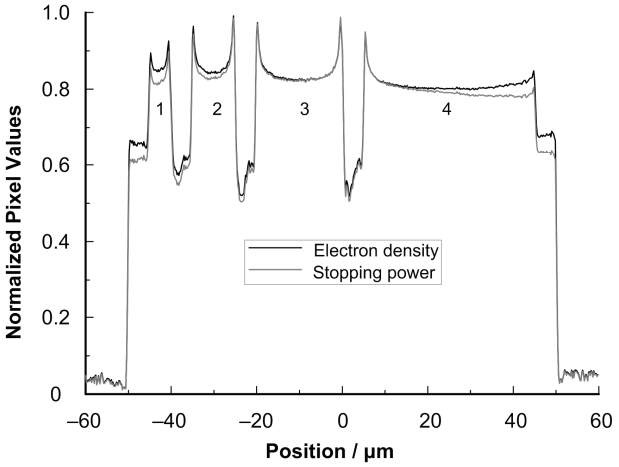

Fig.4 Profiles from the reconstructed images presented in Figs.3 (i) and (l) along the horizontal central line.

4.3 Size analyzing of the cell internal structure

The reconstructed images above are very similar, without size difference of the internal structure. Diameters of the four small cylinders can be calculated by extracting their center image data, by defining the pixel pitch at the difference of relative 50% height as the cylinder diameter (Table 1). Each cylinder keeps almost constant diameter at different energies, except the 0.2 μm difference with one pixel for the Calcium, indicating that the two kinds of reconstruction images do not differ in geometric size. The internal structures in the images are 0.4–0.6 μm (2–3 pixels) larger than those of the actual cylinders, due to the multiple coulomb scattering effects in the proton tracks. This occurs especially near the materials interface, where the protons change their direction and fluence density.

Table 1 Cylinder diameters in reconstruction images in profiles along the horizontal central line*.

Materials	Energy / MeV	Φ5 μm		Φ10 μm		Φ20 μm		Φ40 μm	
		ϕ_S	ϕ_{red}	ϕ_S	ϕ_{red}	ϕ_S	ϕ_{red}	ϕ_S	ϕ_{red}
PMMA	3	5.4	5.4	10.4	10.4	20.6	20.6	40.4	40.4
PMMA	5	5.4	5.4	10.4	10.4	20.6	20.6	40.4	40.4
PMMA	7	5.4	5.4	10.4	10.4	20.6	20.6	40.4	40.4
Calcium	3	5.4	5.4	10.4	10.4	20.6	20.6	40.4	40.4
Calcium	5	5.4	5.4	10.4	10.4	20.6	20.6	40.4	40.4
Calcium	7	5.2	5.4	10.6	10.4	20.6	20.6	40.4	40.4
Average value	—	5.4	5.4	10.4	10.4	20.6	20.6	40.4	40.4
Absolute error	—	0.4	0.4	0.4	0.4	0.6	0.6	0.4	0.4

* ϕ_S, cylinder diameter from stopping power imaging; ϕ_{red}, cylinder diameter from relative electron density imaging.

5 Conclusions

From the above simulations, the proton energy loss and relative electron density integral can be used to reconstruct internal structures of a cell, thus obtaining their correct geometry scales. Except for slight image noise increase in the same cell body, the lower the incident proton energy is, the higher the contrast of the reconstructed image is. Also, the clear lines around the internal structures of the cell can be used to analyze the reconstruction image due to the edge enhancement effect. The PMMA density can be clearly distinguished from water by the proton beam, indicating the density resolving power of the cell imaging in the micro-probe. Therefore, STPMT is a good non-destructive imaging method for cell with low image noise and high image contrast, thus providing a more competitive tool for cell analysis.

References

1 Ivan E, Margio C L K, Sergei A, *et al*. Braz J Phys, 2004, **34:** 804–807.

2 Ren M, Kan J A van, Bettiol A A, *et al*. Nucl Instrm Meth B, 2007, **260:** 124–129.

3 Pontau A E, Antolak A J, Morse D H, *et al*. Nucl Instrum Meth Phys Res B, 1989, **B40:** 646–650.

4 Hanson K M, Bradbury J N, Cannon T M, *et al*. IEEE Trans Nucl Sci, 1978, **NS-25:** 657–660.

5 Frank Watt. Nucl Instrum Meth Phys Res B, 1997, **B130:** 1–8.

6 Saint A, Bench G S, Cholewa M, *et al*. Nucl Instrum Meth Phys Res B, 1991, **B56/57:** 717–721.

7 Formenti P, Breese M B H, Connell S H, *et al*. Nucl

Instrum Meth Phys Res B, 1997, **B130:** 230–236.

8 Antolak A J, Bench G. S, Pontau A E, *et al.* Nucl Instrum Meth Phys Res A, 1994, **A353:** 568–574.

9 Schwertnera M, Sakellarioub A, Reinerta T, *et al.* Ultramicroscopy, 2006, **106:** 574–581.

10 Habchi C, Nguyen D T, Deve G, *et al*. Nucl Instrum Meth B, 2006, **249:** 653–659.

11 Beasley D, Spyrou N M. Nucl Instrum Meth B, 2007, **264:** 323–328.

12 Michelet C, Moretto Ph. Nucl Instrum Meth B, 1999, **150:** 173–178.

13 Moretto Ph, Llabador Y. Nucl Instrum Meth B, 1997, **130:** 324–334.

14 Ren M , Kan J A van, Bettiol A A, *et al*. Nucl Instrum Meth B, 2007, **260:** 124–129.

15 Dollinger G, Datzmann G, Hauptner A, *et al*. Nucl Instrum Meth B, 2003, **210:** 6–13.

16 Li T, Liang J Proc SPIE, 2004, **5370:** 2067–2074.

17 Li T, Liang Z, Mueller K. Nuclear Science Symposium Conference Record, 2003 IEEE, 2003, **4:** 2767–2770.

18 Ivan E, Margio C L K, Sergei A. *et al*. Braz J Phys, 2004, **34:** 804–807.

19 Hanson K M, Bradbury J N, Cannon T M, *et al*. Phys Med Biol, 1981,**26:** 965–983.

20 Zhang C, Hou Q, Gou C, *et al*. Nucl Sci Tech, 2010, **21:** 20–23.

21 Kak A C, Slaney M. Principles of computerized tomographic imaging, http://cobweb.ecn.purdue.edu/~Malcolm /pct/pct-toc. html.